

pubs.acs.org/Macromolecules Article

# Propagation of Elliptically Polarized Light through Ordered Block Copolymers

Chappel J. Sharrock, Ja Eon Cho, Xin Wang, Xiuhong Li, Whitney Loo, Nitash P. Balsara, and Bruce A. Garetz\*



Cite This: Macromolecules 2021, 54, 8372-8380



**ABSTRACT:** The grain structure of an ordered block copolymer material affects its mechanical, electrical, and optical properties, and depolarized light scattering (DPLS) has proven to be a useful method for characterizing this grain structure. In this study, we obtain and analyze DPLS patterns from an ordered diblock copolymer/lithium salt mixture by propagating eight different types of *elliptically* polarized (EP) light through the sample and demonstrate that the patterns are consistent with the ellipsoidal grain model (EGM), which assumes that the sample consists of randomly oriented ellipsoidal grains with optic axes coincident with their shape axes. EP light probes a different population of grains in a sample than either linearly or circularly polarized light and thus may be useful for the characterization of samples with anisotropic grain orientation distributions.

# **■ INTRODUCTION**

Quiescently ordered diblock copolymers (BCPs) typically consist of micrometer-sized grains and concomitant defects. When a neat, disordered BCP sample is cooled below the order-disorder transition temperature, the ordered phase grows by a process of nucleation and growth, consuming the disordered phase until it occupies the entire sample, resulting in a sample filled with randomly oriented grains. This grain structure can affect the mechanical, electrical, and optical properties of the material. When the ordered morphology is lamellar or cylindrical, the grains are optically uniaxial and exhibit form birefringence, and the grain structure can be characterized using depolarized light scattering (DPLS). 1-4 DPLS complements other BCP characterization methods such as small-angle X-ray scattering (SAXS), small-angle neutron scattering (SANS), and electron microscopy (EM).5-13 Although recent studies have shown the potential usefulness of these techniques to determine micron-scale structural features of block copolymers, they are primarily used to determine the ordered morphology on the length scale of the unit cell rather than grain structure. In contrast, all of the DPLS signals from ordered block copolymers arise from the grain structure, as

typical unit cell sizes in block copolymers are much smaller than the wavelength of light.

DPLS can be used to study either oriented samples or quiescently ordered ones. In early work, Keller and co-workers used optical birefringence to show that the ordered phases in block copolymers can be aligned by flow. 14 One may view optical birefringence experiments as DPLS in the limit of large grain size such that all of the depolarized light scattering is coincident with the propagating light beam. In more recent studies, DPLS was used to characterize quiescently ordered block copolymers comprising randomly oriented grains. Since 1998, we have employed the ellipsoidal grain model (EGM) to interpret depolarized scattering patterns from such quiescently ordered samples. 15 This model assumes that randomly oriented

Received: May 25, 2021 Published: September 9, 2021





grains are, on average, ellipsoids of revolution with shape axis coincident with the optic axis. By fitting experimental scattering patterns to this model, we have successfully extracted average grain lengths and widths from a variety of neat BCPs with a variety of compositions (polystyrene-*b*-polyisoprene, polystyrene-*b*-poly(ethylene oxide)), morphologies (lamellar, cylindrical), and molecular weights, as well as mixtures of BCPs with lithium salts. <sup>1,3,15</sup> The extracted grain parameters have been corroborated using transmission electron microscopy (TEM). <sup>16,17</sup> Using a combination of DPLS and SAXS, we were able to characterize a BCP sample with an unusually wide distribution of grain sizes. <sup>4</sup>

Most of the previous work in this field is based on linearly polarized (LP) incident light. In such cases, the depolarized signal is dominated by a subset of grains. For uniaxial systems such as lamellae or cylinders, the measured DPLS signal mainly reflects the structure of grains that are oriented with optic axes that are in the plane perpendicular to the propagation direction, oriented at an angle of about 45° to the polarizer and analyzer axes. In contrast, if DPLS experiments are conducted with circularly polarized (CP) incident light, the DPLS signal equally weights all grains with optic axes that are in the plane perpendicular to the propagation direction. Grain structure is a complex function of both thermodynamic driving forces and nonequilibrium effects such as the free energy of defect formation, extent of flow alignment, and defect annihilation. A more complete description of grain structure may be facilitated using elliptically polarized light in DPLS experiments; by continuously varying the angle,  $\beta$ , between the fast axis of the quarter-wave plate used to control the polarization of the incident beam and the polarizer axis, one can systematically scan the regimes between linearly and circularly polarized (CP) light. DPLS patterns as a function of  $\beta$  will enable the study of different populations of grains

The purpose of this paper is to establish a procedure for analyzing DPLS profiles obtained with an elliptically polarized incident beam. In this early study, we focus on a quiescently ordered block copolymer sample comprising randomly oriented grains. This is a convenient test-bed for establishing our approach, as all populations of grains are "equivalent." Changing  $\beta$  results in tilted DPLS patterns, and we compare experimentally measured tilt angles with theoretical predictions. We show that all of the tilted DPLS scattering patterns arise from the same grain structure. Our work sets the stage for analyzing the grain structure of partially aligned samples with elliptically polarized light.

#### THEORY

Figure 1 shows a schematic of the experimental setup. The incident light travels in the z-direction. The polarizer and analyzer are fixed in the x and y directions, respectively. The two quarter-wave plates, always with perpendicular fast axes, are rotated in tandem by angle  $\beta$ , resulting in the polarization ellipse major axis being rotated by angle  $\beta$ . The experimental scattering pattern is tilted by an angle  $\gamma$ . According to theory,  $\gamma$  should be equal to  $\beta$ . Any point on the scattering pattern can be defined by values of the polar and azimuthal scattering angles  $\theta$  and  $\mu$ .

Within the EGM (assuming randomly oriented grains), whether using LP, CP, or EP light, the scattered intensity can always be decomposed into the sum of two contributions: one that is azimuthally symmetric and the other that has a 4-fold azimuthal symmetry. The relative weights of these two contributions depend on the value of  $\beta$ . For  $\beta$  close to  $0^{\circ}$ , the

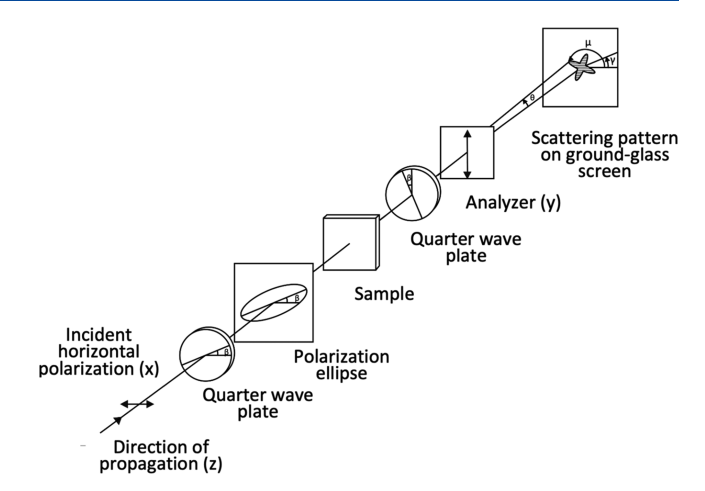


**Figure 1.** Schematic of the optical setup, showing various directions and angles. The fast axes of the quarter-wave plates are indicated by the lines bisecting the plates. The 4-fold symmetry of the scattering pattern has been exaggerated to more clearly show the tilt angle  $\gamma$ .

contributions have roughly equal weights but as  $\beta$  approaches 45°, the symmetric contribution doubles while the 4-fold symmetric contribution goes to zero, according to the functions  $(1 + \sin^2 2\beta)$  and  $(1 - \sin^2 2\beta)$ , respectively.

The incident elliptically polarized beam can be represented by the normalized Jones vector  $\vec{a}_1 = (\hat{x} + e^{i\Phi}\hat{y})/\sqrt{2}$ , where  $\Phi$  is a phase angle between 0 and 360°, and  $\hat{x}$  and  $\hat{y}$  are unit vectors in the x and y directions, respectively. The phase angle  $\Phi$  is equal to  $2\beta$  in our experiments. The resulting scattered intensity becomes

$$I(q, \mu, \beta) = I_0[(1 + \sin^2 2\beta) C_0(q; l, w) + (1 - \sin^2 2\beta) C_4(q; l, w) \cos(4\mu - 4\beta)]$$
(1)

where  $I_0$  is the intensity in the forward direction, q is the magnitude of the scattering vector and is related to the polar scattering angle  $\theta$  by the equation  $q = 4\pi/\lambda \sin(\theta/2)$ , l is the length of the major axis of the ellipsoid, w is the length of the minor axis,  $\mu$  is the azimuthal scattering angle in the scattering plane, and  $\lambda$  is the wavelength of the incident light. The  $C_0(q;l)$ w) component dictates the overall decay of the scattered intensity as a function of q, l, and w. The slower the decay of  $C_0$ vs q, the smaller the average grain size. The  $C_4(q;l, w)$ component is a measure of the depth of the 4-fold angular modulation of the scattering pattern. The larger the magnitude of C4, the more apparent the X-shape of the pattern, and the greater the grain aspect ratio, l/w. As  $\beta$  increases from 0 to 45°, the pattern changes continuously from the 4-fold symmetric LP pattern to the azimuthally symmetric CP pattern. Closed-form expressions for  $C_0$  and  $C_4$  are given in ref 1.

In this study, we have experimentally verified eq 1 using eight different types of *elliptical* polarization (EP) by physically rotating the pair of quarter-wave plates in our DPLS setup, with their fast axes always maintained at right angles to each other, by various angles  $\beta$  ranging from 0 to 40° in increments of 5°.

When elliptically polarized light is made in this way, the orientation of the major axis of the polarization ellipse, the figure swept out by the rotating electric field vector of the light, is tilted relative to the laboratory x-axis by an angle  $\beta$ , as shown in Figure 2.

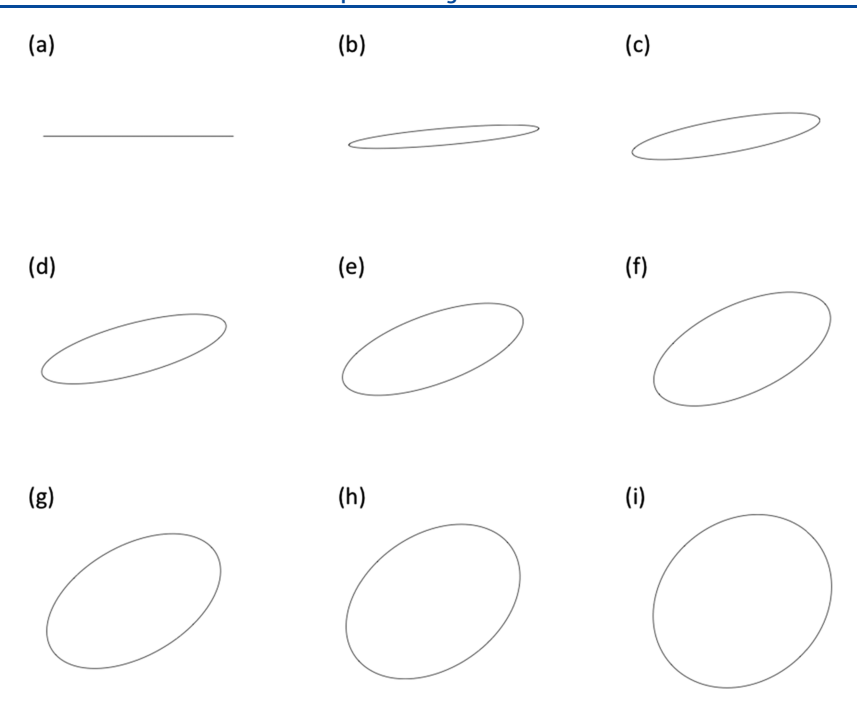


**Figure 2.** Shape and tilt of the polarization ellipse for each polarization state used in this study ( $\beta = 0-40^{\circ}$  in  $5^{\circ}$  steps). Each ellipse has been normalized such that the length of its major axis is unity. State (a) is linear polarization; states (b)–(i) are elliptical polarizations.

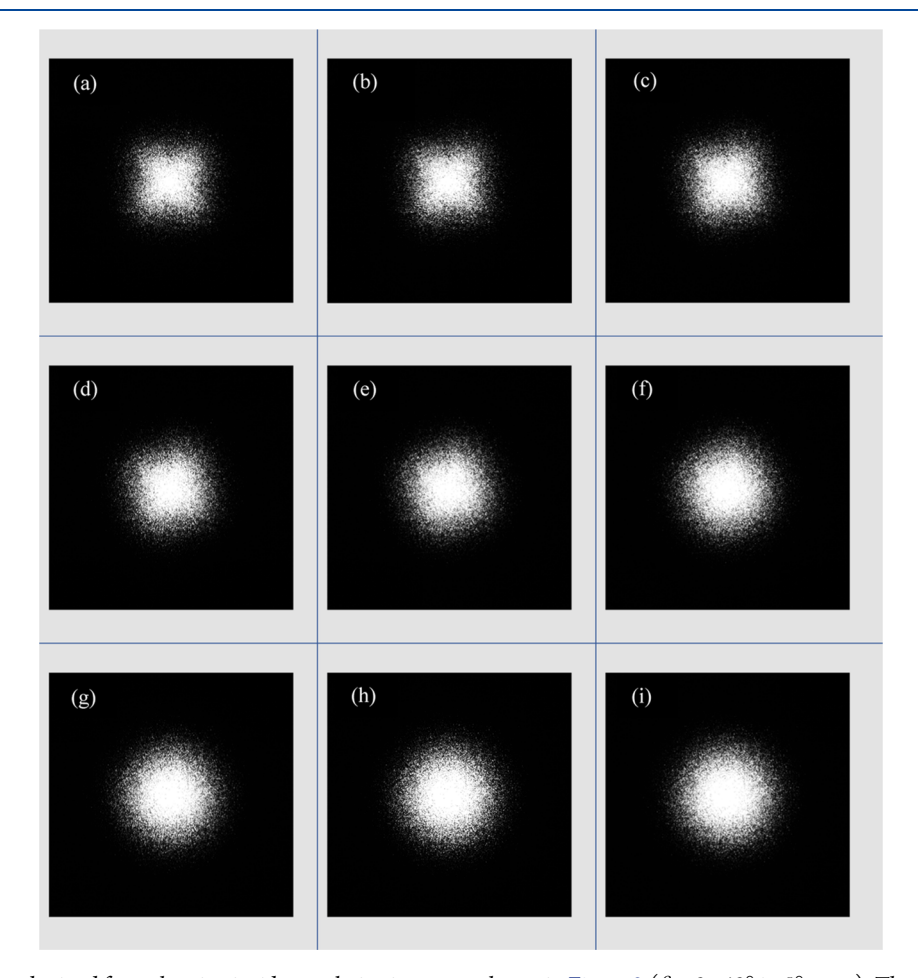


**Figure 3.** DPLS patterns obtained from the nine incident polarization states shown in Figure 2 ( $\beta = 0-40^{\circ}$  in 5° steps). The maximum q value at the side of each image is 1.4  $\mu$ m<sup>-1</sup>.

To obtain estimates of l and w, it is convenient to define  $f_0$  and  $f_4$ , the zeroth and fourth cosine moments of the experimental scattering pattern obtained at angle  $\beta$ 

$$f_0(q, \beta) = \int_0^{2\pi} I(q, \mu, \beta) d\mu$$
  
=  $2\pi I_0 C_0(q; l, w) (1 + \sin^2 2\beta)$  (2)

$$f_4(q, \beta) = \int_0^{2\pi} I(q, \mu, \beta) \cos(4\mu - 4\beta) d\mu$$
  
=  $\pi I_0 C_4(q; l, w) (1 - \sin^2 2\beta)$  (3)

 $f_0$  describes how the azimuthally symmetric contribution to the scattered intensity decays as q increases, while  $f_4$  describes how the 4-fold symmetric contribution varies as q increases. Equations 1 and 3 differ from the equivalent equations in ref 1 because in that earlier study it was assumed that the major axis of the polarization ellipse was fixed at  $45^\circ$  with respect to the x-axis, whereas in this paper, it is tilted by an angle  $\beta$  with respect to the x-axis. The integral in eq 3 can be evaluated using the value of  $\beta$ , the measured tilt of the quarter-wave plates.

## METHODOLOGY

**Sample Preparation and Properties.** This study focused on the analysis and characterization of a polystyrene-b-poly(ethylene oxide) (PS-PEO) diblock copolymer. The sample had a number-average molecular weight of 3.8 kg/mol for PS and 8.2 kg/mol for PEO with a lamellar morphology. The block copolymer was mixed with lithium bis-(trifluoromethanesulfonyl)imide (LiTFSI) to give a salt concentration ratio of 0.025 Li<sup>+</sup> ions to monomer units. The order—disorder temperature ( $T_{\rm ODT}$ ) of the sample was experimentally determined by the birefringence method to be  $127 \pm 2$  °C.

The dried block copolymer/salt mixture was melted into a 1/32" thick Viton rubber spacer with a 3/16" inner diameter at 120 °C (McMaster Carr). The rubber spacer and melted sample were pressed between two quartz disks until an airtight, bubble-free sample was obtained. The quartz disks were positioned in a custom-built aluminum sample holder with a transparent window. Finally, the sample holder was placed within a vacuum-sealed pouch in an argon glovebox and shipped from UC Berkeley to NYU Tandon to run the DPLS experiments.

The temperature of the sample was controlled using an Omega Engineering temperature controller. Before obtaining the scattering patterns, the sample was first heated to 140 °C, above the order-disorder temperature, and held for 1.5 h to fully disorder the sample. It was then quenched to 70 °C and held for an additional 1 h. The DPLS scattering patterns were independent of time after this holding time, indicating that a stable grain structure was obtained. The DPLS data were then collected as a function of  $\beta$  using the apparatus shown in Figure 1. Scattering patterns were stored as 8 bit 801×801-pixel TIFF image files, and intensities were recorded as dimensionless numbers between 0 and 255. To estimate the random error associated with scattering intensities, background patterns were obtained with the sample removed. The calculation of the standard deviation in  $f_0$  obtained from the background patterns yielded a random error of 0.07.

#### RESULTS

**DPLS Scattering Patterns.** Figure 3 displays DPLS patterns obtained as the quarter-wave plates were rotated from  $\beta = 0-40^{\circ}$ . For visual enhancement, the contrast of each image was increased equally by modifying each pixel value,  $\nu$ , by an exponential factor of 2.2 using MATLAB (*i.e.*,  $\nu \rightarrow \nu^{2.2}$ ). It can clearly be seen that as the quarter-wave plates are rotated, the pattern shifts from an X pattern (Pattern (a)) to a nearly circular pattern (Pattern (i)).

All of the scattering patterns in Figure 3 exhibit speckle, the series of fine-grained dots that result from the coherent interference of light waves scattered from different pairs of grains in the sample. The scattered light from a sample can be decomposed into the sum of contributions from single grains (incoherent contribution) and the contributions from grain pairs (coherent contribution). The speckle is not noise; it carries information about the specific arrangement of grains in a particular sample, whereas the incoherent contribution carries information about the average grain structure. The EGM provides an expression for the incoherent scattering, which is equivalent to the scattering pattern obtained by averaging together the patterns from a large ensemble of different samples prepared under the same conditions, for which the coherent contributions average to zero. 15 To aid in the fitting of each experimental scattering pattern to the EGM, we smooth out the high-frequency components of the speckle pattern by applying a spatial Gaussian filter with a fwhm of 12 pixels (=  $0.042 \,\mu\text{m}^{-1}$ ) to each image.1

Using eqs 2 and 3, we extracted values of the cosine moments  $f_0(q, \beta)$  and  $f_4(q, \beta)$  for all nine smoothed scattering patterns, three of which are plotted in Figure 4. We only plot curves

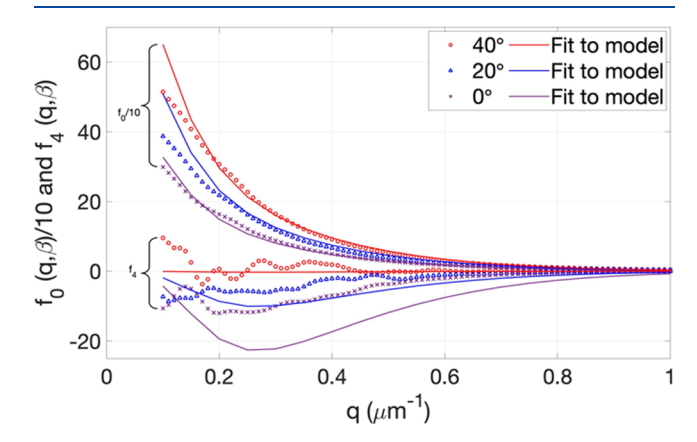


**Figure 4.**  $f_0(q, \beta)$  and  $f_4(q, \beta)$  vs q for three different values of  $\beta$  (symbols) and least-squares fit to EGM with  $l=20~\mu m$  and  $w=3.4~\mu m$  (lines). The error bars are smaller than the symbols.

starting at 0.1  $\mu$ m<sup>-1</sup> because the scattered intensity below 0.1  $\mu$ m<sup>-1</sup> is mixed with the leakage of the incident laser beam through the crossed polarizers. We note that as  $\beta$  increases from 0 to 40°,  $f_0$  curves systematically increase in magnitude while  $f_4$  curves systematically decrease in magnitude, but always remain parallel, in qualitative agreement with the EGM (right-hand sides of eqs 2 and 3).

We define four functions that are helpful for our analysis

$$R_0(q, \beta) = \frac{f_0(q, \beta)}{f_0(q, 0)} = 1 + \sin^2 2\beta;$$

$$R_{0,av}(\beta) = \langle R_0(q, \beta) \rangle_q$$
(4)

$$R_{4}(q, \beta) = \frac{f_{4}(q, \beta)}{f_{4}(q, 0)} = 1 - \sin^{2} 2\beta;$$

$$R_{4,av}(\beta) = \langle R_{4}(q, \beta) \rangle_{q}$$
(5)

 $R_0$  and  $R_4$  are ratios between the curves shown in Figure 4 and the  $\beta = 0^{\circ}$  curve, *i.e.*,  $R_0$  is the ratio of the zeroth cosine moment obtained from each type of elliptically polarized light with the zeroth cosine moment obtained with linearly polarized light, and  $R_4$  is the ratio of the fourth cosine moment obtained from each type of elliptically polarized light with the fourth cosine moment obtained with linearly polarized light.  $R_{0,av}$  and  $R_{4,av}$  are the functions  $R_0$  and  $R_4$  averaged over all values of q. The brackets parentheses indicate an average over all values of q. According to the EGM, these ratios should be independent of q and equal to 1  $+\sin^2 2\beta$  and  $1-\sin^2 2\beta$ , respectively. In other words, the ratios should be constant, independent of the sample, and dependent only on the state of EP used. Any major deviations from a constant is an indication of a violation of the EGM, such as a nonrandom grain orientation distribution. From the  $\beta = 0^{\circ}$  (LP) pattern, we least-squares fit the values of  $f_0(q, 0)$  and  $f_4(q, 0)$  to the EGM (eq 1) as shown by the lines in Figure 4, yielding average grain parameters  $l = 20 \mu m$  and  $w = 3.4 \mu m$ . We also plot the predicted  $f_0(q, \beta)$  and  $f_4(q, \beta)$  curves for two other values of  $\beta$ , based on the right-hand sides of eqs 2 and 3. We note that the agreement between  $f_0(q, \beta)$  and the EGM is excellent. The model also correctly captures the factor of 10 difference in magnitude between  $f_0(q, \beta)$  and  $f_4(q, \beta)$ , as well as the sign of  $f_4(q,\beta)$ . As we have pointed out in previous publications, <sup>1,3</sup> the  $f_4$ mismatch is exaggerated because the  $f_4$  curves in Figure 4 are magnified by a factor of 10 compared to the  $f_0$  curves. In addition, the  $f_4$  mismatch lessens as  $\beta$  increases because the  $\beta$ dependence begins to dominate over the  $C_4$  dependence. Given that we are fitting scattering patterns from a complex sample using a model with only three parameters  $(l, w, and I_0)$ , it is quite remarkable that the fit is as good as it is.

In Figure 5, we have plotted the values of  $R_0(q, \beta)$  and  $R_4(q, \beta)$  vs q for three scattering patterns. We note that, with the

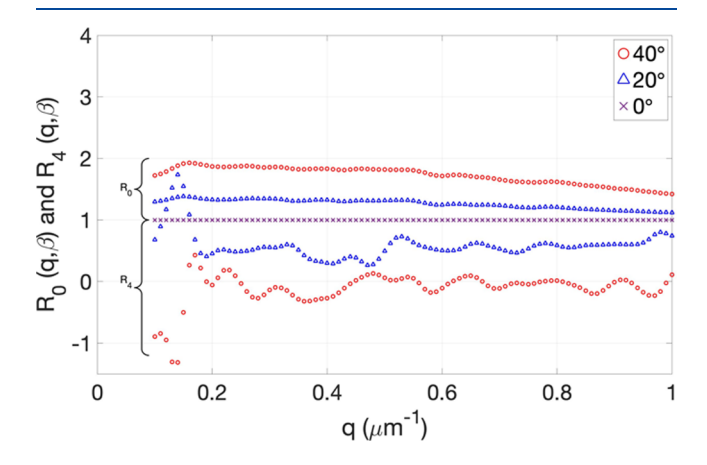


**Figure 5.**  $R_0(q, \beta)$  and  $R_4(q, \beta)$  vs q for different values of  $\beta$ . The error bars are smaller than the symbols. For  $\beta = 0^\circ$ , the  $R_0$  and  $R_4$  curves are coincident and equal to unity.

exception of some unexpected peaks in  $R_4(q,\beta)$  between 0.1 and 0.2  $\mu\text{m}^{-1}$ , all of these curves are, to a good approximation, horizontal lines, *i.e.*, independent of q, as predicted by theory. In addition, as  $\beta$  increases from 0 to 40°, the  $R_0$  curves systematically increase in magnitude while the  $R_4$  curves systematically decrease in magnitude, also in qualitative agreement with theory. The mild undulations seen in the  $f_4$  and  $R_4$  curves are probably a residual effect of speckle that was not smoothed out by the Gaussian filtering and not averaged out during the integration of  $I(q,\mu,\beta)$  over  $\mu$ . The large peaks in  $R_4(q,\beta)$  between 0.1 and 0.2  $\mu\text{m}^{-1}$  might be an indication of a nonrandom orientational distribution of large grains. Such complexities will be the subject of a future study. To sidestep this complexity here, we calculate  $R_{0,av}$  and  $R_{4,av}$  by averaging the values of  $R_0(q,\beta)$  and  $R_4(q,\beta)$  between q=0.2 and  $1.0~\mu\text{m}^{-1}$ .

Tilt of the X Pattern and Extraction of  $R_{4,av}$ . The DPLS scattering pattern at  $\beta=0^\circ$  has an untilted X-shape. As  $\beta$  increases, the X pattern tilts and the patterns become more azimuthally symmetric. The azimuthal asymmetry is lost entirely when  $\beta=45^\circ$  (circular polarization). We have defined  $\gamma$  to be the tilt of the DPLS scattering profile for a given value of  $\beta$ . It is, however, difficult to determine  $\gamma$  by simple visual inspection of the data. We thus devised a quantitative method for determining  $\gamma$ .

In theory, the tilt of the X pattern should be equal to  $\beta$ . However, we have chosen to measure the experimental tilt of the scattering pattern independently by replacing  $\beta$  in the integral in eq 3 by a variable angle  $\gamma$  as shown in eq 6. The optimum value of  $\gamma$ , which we denote as  $\gamma_{\text{opt}}$  is the one that maximizes the magnitude of  $f_4$ , *i.e.*, the value that maximizes the depth of the fourfold modulation of the scattering pattern. According to theory,  $\gamma_{\text{opt}}$  should be equal to  $\beta$ .

$$f_4(q, \beta, \gamma) = \int_0^{2\pi} I(q, \mu, \beta) \cos(4\mu - 4\gamma) d\mu$$
 (6)

To maximize a function such as  $f_4$ , we could choose to maximize its value at a particular value of q, but that would be rather arbitrary. We instead define the following two quantities

$$R_4(q, \beta, \gamma) = \frac{f_4(q, \beta, \gamma)}{f_4(q, 0)}; \ R_{4,av}(\beta, \gamma) = \langle R_4(q, \beta, \gamma) \rangle_q$$

For a particular value of  $\gamma$ , we compute the  $f_4$  of a tilted pattern, obtained at a particular value of  $\beta$ , and the  $f_4$  of the untilted X pattern ( $\beta=0^{\circ}$ ). We then take the ratio of these two functions and average the resulting ratio of functions,  $R_4$ , over the q range of  $0.2-1.0~\mu\text{m}^{-1}$  at intervals of  $0.01~\mu\text{m}^{-1}$ . We have thus reduced the function  $f_4(q, \beta, \gamma)$  to a single number,  $R_{4,\text{av}}(\beta, \gamma)$ . The optimum value of  $\gamma$  is the one that maximizes  $R_{4,\text{av}}(\beta, \gamma)$ , *i.e.*, the one that maximizes the fourfold modulation of the scattering pattern. Mathematically, we require that

$$\left(\frac{\mathrm{d}R_{4,\mathrm{av}}(\beta,\gamma)}{\mathrm{d}\gamma}\right)_{\gamma=\gamma_{\mathrm{opt}}} = 0$$
(8)

In addition, the best value of  $R_{4,av}$  for a given value of  $\beta$  is  $R_{4,av}(\beta, \gamma_{opt})$ . If the BCP scatters according to the EGM,  $R_0$  and  $R_4$  will have values that are independent of q and will be equal to  $(1 + \sin^2 2\beta)$  and  $(1 - \sin^2 2\beta)$ , respectively, and  $\gamma_{opt}$  will be equal to  $\beta$ .

We chose a range of  $\gamma$  values in the vicinity of the measured value of  $\beta$  and used eqs 6 and 7 to compute the value of  $R_{4,av}$  for

each value of  $\gamma$ . Figure 6 shows plots of  $R_{4,av}$  vs  $\gamma$  for each of six forms ( $\beta = 5-30^{\circ}$ ) of EP light. We then used eq 8 to determine

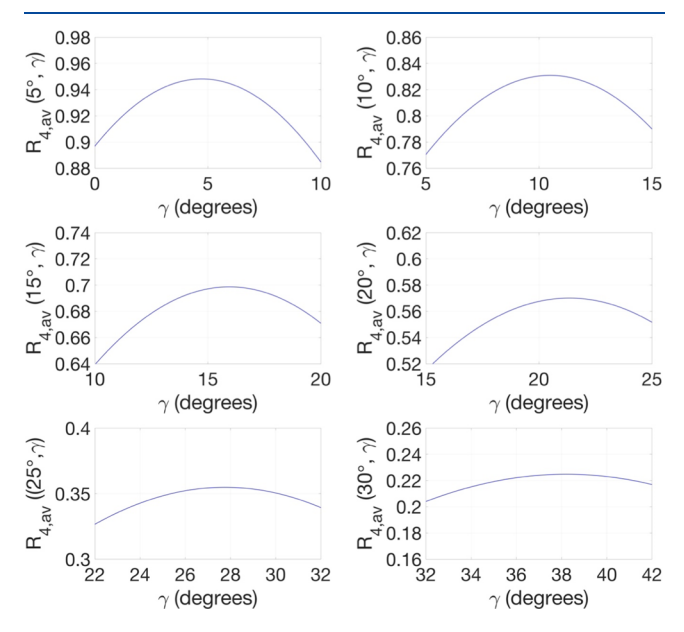


**Figure 6.**  $R_{4\text{-av}}$  vs  $\gamma$  from elliptically polarized patterns ( $\beta = 5-30^{\circ}$ ).

the values of  $\gamma_{\rm opt}$  and  $R_{\rm 4,av}(\beta, \gamma_{\rm opt})$ . The uncertainty in  $\gamma_{\rm opt}$  was estimated by noting the range over which  $R_{\rm 4,av}$  was reduced by  $\pm 0.01$  from its maximum value. Figure 7 shows a plot of  $\gamma_{\rm opt}$  vs  $\beta$ .

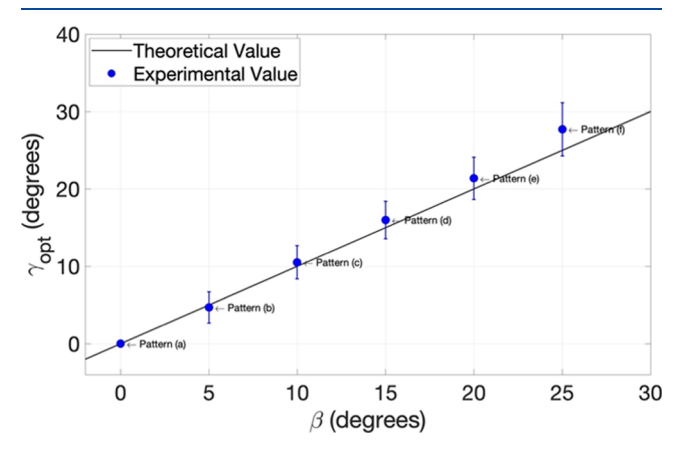


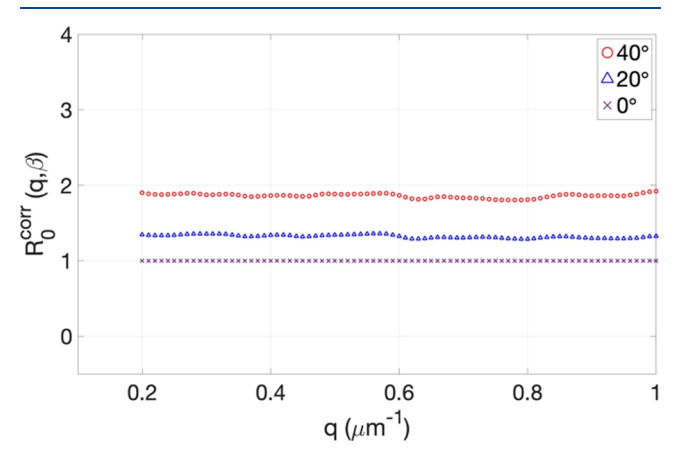
**Figure 7.** Comparison between  $\gamma_{\rm opt}$  and  $\beta$  angles.

As  $\beta$  increases and the scattering pattern becomes more symmetric, the curvature of the plot gets lower, and the value of  $\gamma_{\rm opt}$  becomes less precise, such that we are confident of the  $\gamma_{\rm opt}$  values up to  $\beta=25^\circ$ . It is evident that the experimentally determined tilts of the DPLS patterns are in reasonable agreement with the theoretical prediction  $\gamma_{\rm opt}=\beta$ .

**Extraction and Analysis of**  $R_0$ . It can be seen from Figure 5 that the values of  $R_0$  decrease at large q by about 10%. We believe that this decline is the result of stray background light reaching the ground glass screen, resulting in a systematic offset to the values of  $f_0$ . A similar fall-off was observed in  $R_0(q, 45^\circ)$  in ref 1, *i.e.*, the ratio of the zeroth cosine moment obtained with CP incident light to that obtained with LP light. The offset was corrected by subtracting a constant, b, from  $f_0$  as follows

$$R_0^{\text{corr}}(q,\beta) = \frac{f_0(q,\beta) - b}{f_0(q,0) - b}; R_{0,\text{av}}^{\text{corr}}(\beta) = \langle R_0^{\text{corr}}(q,\beta) \rangle_q$$
(9)

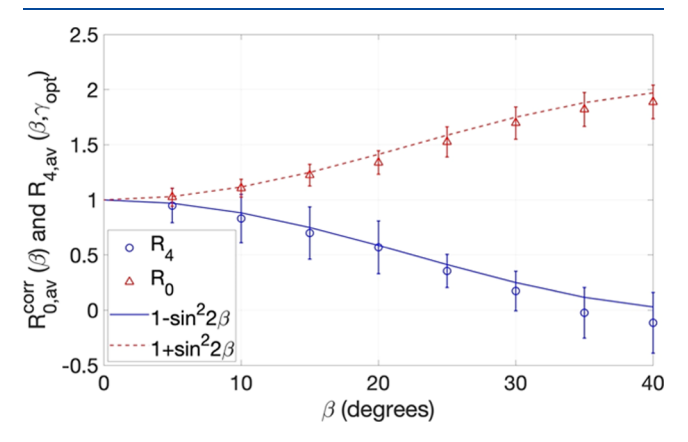
It was found that the value of b that produced the most constant, q-independent  $R_0$  was 1.5. This means that the value of the intensity of each pixel had an additional  $1.5/2\pi = 0.24$  units (out of a maximum 255 units) due to stray-light exposure during measurements. All  $R_0$  values have been corrected in this way to provide the best fit to the experimental results. Figure 8 shows



**Figure 8.**  $R_0^{corr}(q, \beta)$  vs q, from elliptically polarized patterns ( $\beta = 20$  and  $40^{\circ}$ ).

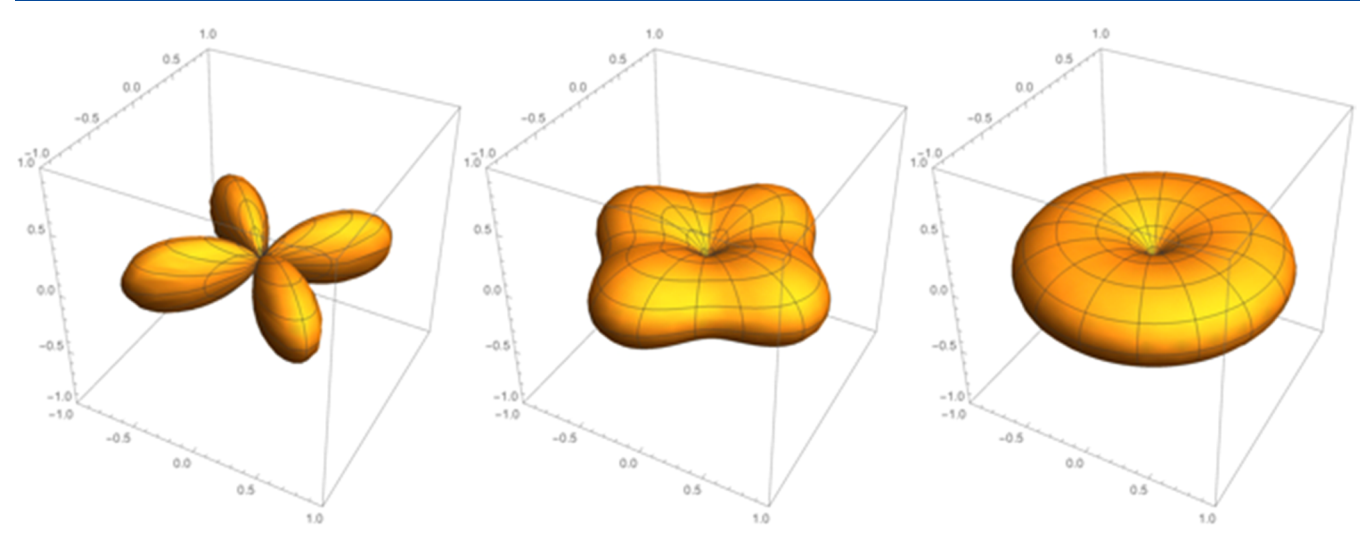
plots of  $R_0^{\rm corr}$  vs q using corrected  $R_0$  values. This correction was not necessary for  $f_4$  because any constant background in the scattered intensity averages to zero after the  $\mu$ -integration in eq 6. The error associated with  $R_{0,{\rm av}}^{\rm corr}$  was obtained by combining the standard deviation of each respective  $R_{0,{\rm av}}^{\rm corr}$  value and the random error associated with the background patterns. The error associated with  $R_{4,{\rm av}}$  was obtained by calculating the standard deviation of each respective  $R_{4,{\rm av}}$  value.

Figure 9 plots the average values of  $R_{0,av}^{corr}(\beta)$  and  $R_{4,av}(\beta, \gamma_{opt})$  as a function of  $\beta$  for each scattering pattern, as well as the



**Figure 9.**  $R_{0,\mathrm{av}}^{\mathrm{corr}}(\beta)$  and  $R_{4,\mathrm{av}}(\beta, \gamma_{\mathrm{opt}})$  vs  $\beta$ , theoretically and experimentally obtained values.

functions  $1+\sin^2 2\beta$  and  $1-\sin^2 2\beta$ , which  $R_{0,\mathrm{av}}$  and  $R_{4,\mathrm{av}}$  are predicted to equal, respectively, according to the EGM. For patterns for which we could not obtain a reliable value of  $\gamma_{\mathrm{opt}}$  *i.e.*, for  $\beta \geq 30^\circ$ , we have plotted the value of  $R_{4,\mathrm{av}}(\beta)$ . The experimental values of  $R_{0,\mathrm{av}}^{\mathrm{corr}}$  and  $R_{4,\mathrm{av}}$  agree with the theoretically expected functions within the experimental error estimates.



**Figure 10.** Polar plots of weighted grain orientations that contribute to DPLS light scattering. From left to right: using LP, EP ( $\beta = 30^{\circ}$ ), and CP. The two horizontal axes are the x and y linear polarizer directions, and the vertical axis, z, is the direction of propagation of the incident light.

#### CONCLUSIONS

We have demonstrated that depolarized scattering patterns from a BCP/Li<sup>+</sup> salt mixture can be obtained using eight types of elliptically polarized light and that the shape and tilt of the patterns are consistent with the EGM. Different elliptical polarizations probe different populations of grains from both circular and linear polarizations, thereby furthering the possibilities for understanding grain structure and growth. This can be seen in Figure 10, which compares the polar plots of the weighted grain orientations that contribute to the DPLS patterns obtained with different types of polarization. A combination of linearly, elliptically, and circularly polarized light can be used within depolarized light scattering studies to probe the different populations of grains, thereby providing the most complete picture of the grain orientation distribution.

The extent to which and the way in which the experimentally obtained scattering pattern deviates from the predictions of the EGM provide indications to the ways in which the sample is anisotropic with respect to grain orientation, shape, or size distribution. One approach would be to calculate the residual between the experimental DPLS pattern and the pattern formed by the extracted  $f_0$  and  $f_4$  components. Analysis of the differential changes in the residual pattern (size, shape, symmetry, orientation) with respect to the change in polarization state (i.e., the change in  $\beta$ ) would identify which populations of grains in the sample are deviating from the EGM and how they are deviating. This is similar to the way we analyzed partially aligned samples in ref 20, where besides the  $f_0$  and  $f_4$  components, we observed a 2-fold symmetric component, although that study was limited to LP light.

This study experimentally supported the ellipsoidal grain model and demonstrated that this model is robust enough to allow the characterization of grains with varying polarizations of light.

# AUTHOR INFORMATION

# **Corresponding Author**

Bruce A. Garetz — Department of Chemical and Biomolecular Engineering, NYU Tandon School of Engineering, Brooklyn, New York 11201, United States; orcid.org/0000-0002-3141-7840; Email: bgaretz@nyu.edu

#### **Authors**

Chappel J. Sharrock – Department of Chemical and Biomolecular Engineering, NYU Tandon School of Engineering, Brooklyn, New York 11201, United States

Ja Eon Cho — Department of Chemical and Biomolecular Engineering, NYU Tandon School of Engineering, Brooklyn, New York 11201, United States

Xin Wang — Department of Chemical and Biomolecular Engineering, NYU Tandon School of Engineering, Brooklyn, New York 11201, United States; orcid.org/0000-0002-8643-0196

Xiuhong Li — Department of Chemical and Biomolecular Engineering, NYU Tandon School of Engineering, Brooklyn, New York 11201, United States

Whitney Loo – Department of Chemical and Biomolecular Engineering, University of California, Berkeley, Berkeley, California 94720, United States

Nitash P. Balsara — Department of Chemical and Biomolecular Engineering, University of California, Berkeley, Berkeley, California 94720, United States; Environmental Energy Technologies Division and and Materials Science Division, Lawrence Berkeley National Laboratory, Berkeley, California 94720, United States; Occid.org/0000-0002-0106-5565

Complete contact information is available at: https://pubs.acs.org/10.1021/acs.macromol.1c01134

#### **Author Contributions**

C.J.S. and J.E.C. contributed equally to the manuscript. The manuscript was written through the contributions of all authors. All authors have given approval to the final version of the manuscript.

#### Notes

The authors declare no competing financial interest.

# ACKNOWLEDGMENTS

Primary funding for this work was provided by the National Science Foundation through Awards DMR-1904537 and DMR-1904508. Any opinions, findings, and conclusions or recommendations expressed in this paper are those of the authors and do not necessarily reflect the views of the National Science Foundation.

Macromolecules Article pubs.acs.org/Macromolecules

# ■ NOMENCLATURE

#### **Abbreviations**

**BCP** block copolymer CP circularly polarized **DPLS** depolarized light scattering **EGM** ellipsoidal grain model EM electron microscopy EP elliptically polarized full width at half-maximum fwhm

LiTFSI lithium bis(trifluoromethanesulfonyl)imide

LP linearly polarized

ODT order-to-disorder transition **PEO** poly(ethylene oxide)

PS polystyrene

small-angle neutron scattering **SANS SAXS** small-angle X-ray scattering TIFF tagged image file format

# SYMBOLS

complex unit vector for incident polarization state,  $\vec{a}_1$ dimensionless

b constant for stray-light correction to cosine moments, dimensionless

 $C_0(q; l, w)$ azimuthally symmetric component of theoretical scattering intensity, dimensionless

 $C_4(q;l,w)$ 4-fold modulated component of theoretical scattering intensity, dimensionless

 $f_0(q, \beta)$ zeroth cosine moment of experimental EP scattered intensity, dimensionless

 $f_4(q, \beta)$ fourth cosine moment of experimental EP scattered intensity, dimensionless

 $f_4(q, \beta, \gamma)$ fourth cosine moment of experimental EP scattered intensity calculated assuming a tilt angle of  $\gamma$ , dimensionless

 $I_0$ scattered depolarized intensity in forward direction with LP light, dimensionless

 $I(q, \mu, \beta)$ scattered depolarized intensity as a function of q,  $\mu$ , and  $\beta$ , dimensionless

characteristic grain length in ellipsoidal grain model, um

magnitude of scattering vector,  $\mu \text{m}^{-1}$ 

 $\tilde{R}_0(q,\beta)$ ratio of  $f_0$  obtained from the EP pattern at angle  $\beta$  to that obtained from the LP pattern, dimensionless

 $R_{0,av}(\beta)$ value of  $R_0$  averaged over q, dimensionless  $R_0$  corrected for background light, dimensionless

 $R_0^{\text{corr}}(q, \beta)$   $R_{0,\text{av}}^{\text{corr}}(\beta)$ value of  $R_0^{\text{corr}}$  averaged over q, dimensionless  $R_4(q, \beta)$ ratio of  $f_4$  obtained from the EP pattern at angle  $\beta$  to

that obtained from the LP pattern, dimensionless  $R_{4,av}(\beta)$ value of  $R_4(q, \beta)$  averaged over q, dimensionless

 $R_4(q, \beta, \gamma)$ ratio of  $f_4$  obtained from the EP pattern at angle  $\beta$  to that obtained from the LP pattern, assuming a tilt angle of  $\gamma$ , dimensionless

value of  $R_4(q, \beta, \gamma)$  averaged over q, dimensionless  $R_{4,av}(\beta, \gamma)$  $T_{\text{ODT}}$ order-disorder transition temperature, Kelvin characteristic grain width in the ellipsoidal grain model,  $\mu$ m

â unit vector representing x-polarized light, dimensionless

unit vector representing y-polarized light, dimenŷ

direction of propagation of the incident light beam, z

#### **GREEK LETTERS**

β tilt angle of quarter-wave plate, degrees

variable tilt angle used to compute  $f_4$  from a tilted scattering γ pattern, degrees

optimum calculated tilt angle of scattering pattern, degrees polar angle of scattered ray, degrees

λ wavelength of the incident light, nm

azimuthal angle of scattered ray, degrees

Φ phase angle in defining elliptical polarization state, degrees

#### REFERENCES

- (1) Wang, X.; Li, X.; Loo, W.; Newstein, M. C.; Balsara, N. P.; Garetz, B. A. Depolarized Scattering from Block Copolymer Grains using Circularly Polarized Light. Macromolecules 2017, 50, 5122-5131.
- (2) Li, X.; Loo, W. S.; Jiang, X.; Wang, X.; Galluzzo, M. D.; Mongcopa, K. I.; Wang, A. A.; Balsara, N. P.; Garetz, B. A. Confined versus Unconfined Crystallization in Block Copolymer/Salt Mixtures Studied by Depolarized Light Scattering. Macromolecules 2019, 52, 982-991.
- (3) Wang, X.; Thelen, J. L.; Teran, A. A.; Chintapalli, M.; Nakamura, I.; Wang, Z. G.; Newstein, M. C.; Balsara, N. P.; Garetz, B. A. Evolution of Grain Structure during Disorder-to-Order Transitions in a Block Copolymer/Salt Mixture Studied by Depolarized Light Scattering. Macromolecules 2014, 47, 5784-5792.
- (4) Wang, X.; Chintapalli, M.; Newstein, M. C.; Balsara, N. P.; Garetz, B. A. Characterization of a Block Copolymer with a Wide Distribution of Grain Sizes. Macromolecules 2016, 49, 8198-8208.
- (5) Shibayama, M.; Hashimoto, T. Small-Angle X-Ray-Scattering Analyses of Lamellar Microdomains Based on a Model of One-Dimensional Paracrystal with Uniaxial Orientation. Macromolecules **1986**, 19, 740-749.
- (6) Ryu, H. J.; Fortner, D. B.; Lee, S.; Ferebee, R.; De Graef, M.; Misichronis, K.; Avgeropoulos, A.; Bockstaller, M. R. Role of Grain Boundary Defects During Grain Coarsening of Lamellar Block Copolymers. Macromolecules 2013, 46, 204-215.
- (7) Ryu, H. J.; Fortner, D. B.; Rohrer, G. S.; Bockstaller, M. R. Measuring Relative Grain-Boundary Energies in Block-Copolymer Microstructures. Phys. Rev. Lett. 2012, 108, No. 107801.
- (8) Campbell, I. P.; He, C. L.; Stoykovich, M. P. Topologically Distinct Lamellar Block Copolymer Morphologies Formed by Solvent and Thermal Annealing. ACS Macro Lett. 2013, 2, 918-923.
- (9) Campbell, I. P.; Lau, G. J.; Feaver, J. L.; Stoykovich, M. P. Network Connectivity and Long-Range Continuity of Lamellar Morphologies in Block Copolymer Thin Films. Macromolecules 2012, 45, 1587-1594.
- (10) Hashimoto, T.; Nagatoshi, K.; Todo, A.; Hasegawa, H.; Kawai, H. Domain-Boundary Structure of Styrene-Isoprene Block Copolymer Films Cast from Toluene Solutions. *Macromolecules* **1974**, *7*, 364–373.
- (11) Ryu, H. J.; Sun, J.; Avgeropoulos, A.; Bockstaller, M. R. Retardation of Grain Growth and Grain Boundary Pinning in Athermal Block Copolymer Blend Systems. Macromolecules 2014, 47, 1419-
- (12) Hu, X. C.; Gido, S. P.; Russell, T. P.; Iatrou, H.; Hadjichristidis, N.; Abuzaina, F. M.; Garetz, B. A. Grain growth kinetics of A(n)B(n)star block copolymers in supercritical. carbon dioxide. Macromolecules 2005, 38, 4719-4728.
- (13) Olsen, B. D.; Segalman, R. A. Structure and thermodynamics of weakly segregated rod-coil block copolymers. Macromolecules 2005, 38,
- (14) Folkes, M. J.; Keller, A. The birefringence and mechanical properties of a 'single crystal' from a three-block copolymer. Polymer 1971, 12, 222-236.
- (15) Newstein, M. C.; Garetz, B. A.; Balsara, N. P.; Chang, M. Y.; Dai, H. J. Growth of grains and correlated grain clusters in a block copolymer melt. Macromolecules 1998, 31, 64-76.
- (16) Garetz, B. A.; Balsara, N. P.; Dai, H. J.; Wang, Z.; Newstein, M. C.; Majumdar, B. Orientation correlations in lamellar block copolymers. Macromolecules 1996, 29, 4675-4679.

- (17) Chang, M. Y.; Abuzaina, F. M.; Kim, W. G.; Gupton, J. P.; Garetz, B. A.; Newstein, M. C.; Balsara, N. P.; Yang, L.; Gido, S. P.; Cohen, R. E.; Boontongkong, Y.; Bellare, A. Analysis of grain structure in partially ordered block copolymers by depolarized light scattering and transmission electron microscopy. *Macromolecules* **2002**, *35*, 4437–4447.
- (18) Thelen, J. L.; Teran, A. A.; Wang, X.; Garetz, B. A.; Nakamura, I.; Wang, Z. G.; Balsara, N. P. Phase Behavior of a Block Copolymer/Salt Mixture through the Order-to-Disorder Transition. *Macromolecules* **2014**, 47, 2666–2673.
- (19) Yuan, R.; Teran, A. A.; Gurevitch, I.; Mullin, S. A.; Wanakule, N. S.; Balsara, N. P. Ionic Conductivity of Low Molecular Weight Block Copolymer Electrolytes. *Macromolecules* **2013**, *46*, 914–921.
- (20) Abuzaina, F. M.; Garetz, B. A.; Mody, J. U.; Newstein, M. C.; Balsara, N. P. Birefringence and depolarized light scattering from ordered block copolymers with anisotropic distributions of grain orientations produced by shear flow. *Macromolecules* **2004**, *37*, 4185–4195.